



## X-ray imaging and 3DXRD - Fundamentals and Applications

Oddershede, Jette

*Publication date:*  
2010

*Document Version*  
Publisher's PDF, also known as Version of record

[Link back to DTU Orbit](#)

*Citation (APA):*  
Oddershede, J. (2010). *X-ray imaging and 3DXRD - Fundamentals and Applications*. Paper presented at 2010 LANSCE Neutron School, Los Alamos, New Mexico, United States.

---

### General rights

Copyright and moral rights for the publications made accessible in the public portal are retained by the authors and/or other copyright owners and it is a condition of accessing publications that users recognise and abide by the legal requirements associated with these rights.

- Users may download and print one copy of any publication from the public portal for the purpose of private study or research.
- You may not further distribute the material or use it for any profit-making activity or commercial gain
- You may freely distribute the URL identifying the publication in the public portal

If you believe that this document breaches copyright please contact us providing details, and we will remove access to the work immediately and investigate your claim.

# 4D studies in materials science

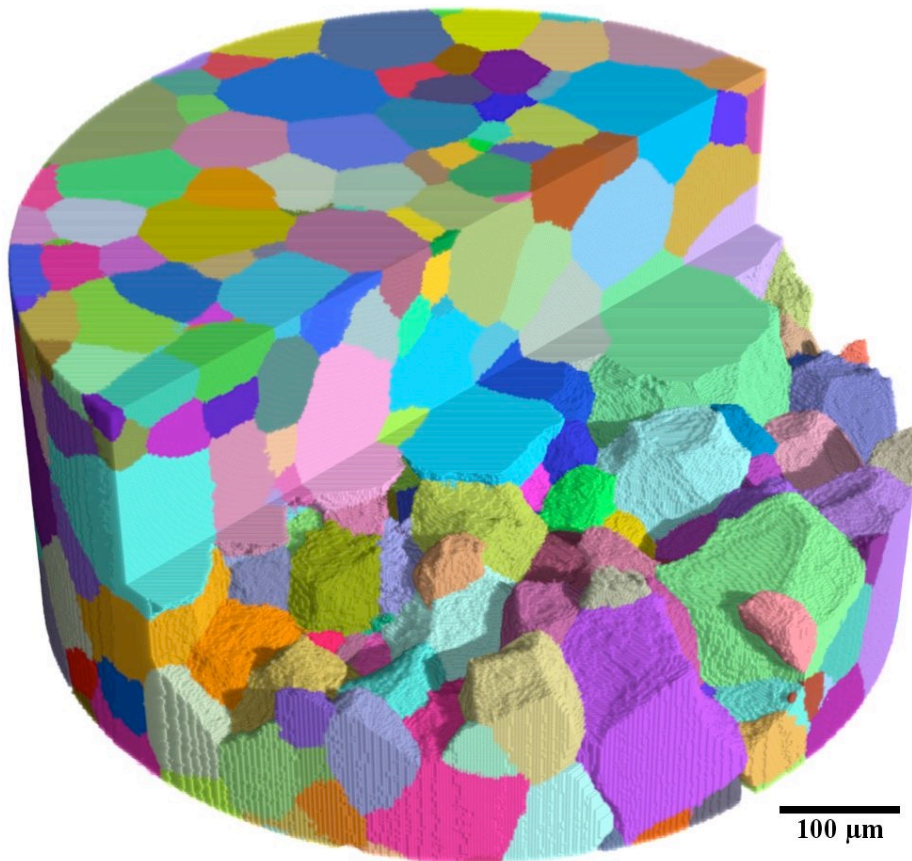
- notes for the Neutron School at Los Alamos, August 2010

Henning Friis Poulsen

[hfpo@risoe.dtu.dk](mailto:hfpo@risoe.dtu.dk)

Jette Oddershede

[jeto@risoe.dtu.dk](mailto:jeto@risoe.dtu.dk)



These notes are a revised version of Chapter 9 in *Advanced tomographic methods in materials research and engineering* (Banhardt, Oxford, 2008)

## Three Dimensional X-Ray Diffraction (3DXRD)

In Nature most materials, such as rocks, ice, sand and soil, appear as aggregates composed of a set of crystalline elements. Similarly, many man-made materials are polycrystalline, *e.g.* metals, alloys and ceramics. So are drugs, bones and trace particles relevant to environmental matters.

Remarkably, until recently no non-destructive methods existed for providing comprehensive 3-dimensional information on the structure and dynamics of polycrystals at the scale of the individual microstructural elements (the grains, sub-grains, particles or domains). X-ray and neutron diffraction have been confined to two limiting cases: powder diffraction, which averages over the elements, and diffraction on single crystals. Most real world materials occur as heterogeneous aggregates with substantial internal structure, and thus fall between these two extremes. Absorption contrast tomography is not sensitive to crystalline lattice, and as such cannot visualise the elements within a mono-phase material. Local information has been provided by tools such as optical, electron, ion beam and scanning probe microscopy. However, these methods probe the near surface regions only. Hence, the characterization is only two-dimensional and prohibits studies of the bulk dynamics.

Three-Dimensional X-Ray Diffraction (3DXRD) is a novel technique, aiming at a fast and non-destructive characterization of the individual elements within millimetre to centimetre-sized specimens. It is based on two principles: the use of highly penetrating hard X-rays from a synchrotron source (X-ray energies above 30 keV) and the application of “tomographic” reconstruction algorithms for the analysis of the diffraction data. In favourable cases, the position, morphology, phase, and crystallographic orientation can be derived for hundreds of elements simultaneously as well as their elastic strains. Furthermore, the dynamics of the individual elements can be monitored during typical processes such as deformation or annealing. Hence, for the first time information on the interaction between elements can be obtained directly. The provision of such data is vital in order to extend beyond state-of-the-art structural models.

In this note the 3DXRD methodology will be outlined with focus on characterising grains and orientations. Notably, in a 3DXRD experiment one must prioritise between spatial, angular and time resolution. This has led to a variety of 3DXRD strategies, which in the following will be summarised as four *standard modes of operation*. The first two modes enable fast measurements of the *average characteristics* of each grain (such as their center-of-mass position, volume, average orientation and/or average value of strain tensor components), while the exact location of the grain boundaries is unknown. The latter two enable full 3D mappings of grains and orientations. For general reference, see [1].

In the following, initially the 3DXRD setup will be presented and 3DXRD strategies discussed. Then the standard modes of operation are presented in more detail with emphasis on reconstruction principles and with selected examples of use. Next, a novel method called diffraction contrast tomography (DCT) is presented – this is related to 3DXRD in the same way as bright-field and dark-field images are in transmission electron microscopy.

Alternative approaches to provision of 3D maps based on X-ray diffraction exist. These are based on inserting wires [2], slits [3] or collimators [4] between the sample and the detector and scanning the sample with respect to these elements. Such methods will be slower than the tomographic

approach of 3DXRD, but they may be associated with other advantages, such as improved options for measuring the local elastic strain. In particular we mention the technique of “differential-aperture X-ray microscopy” [2] by Larson *et al.* Using a polychromatic microbeam with energies of 8-20 keV and scanning a wire, they have demonstrated sub-micrometre resolution in 3D. For a comparison of methods see *e.g.* [5].

## 1. Basic set-up and strategy

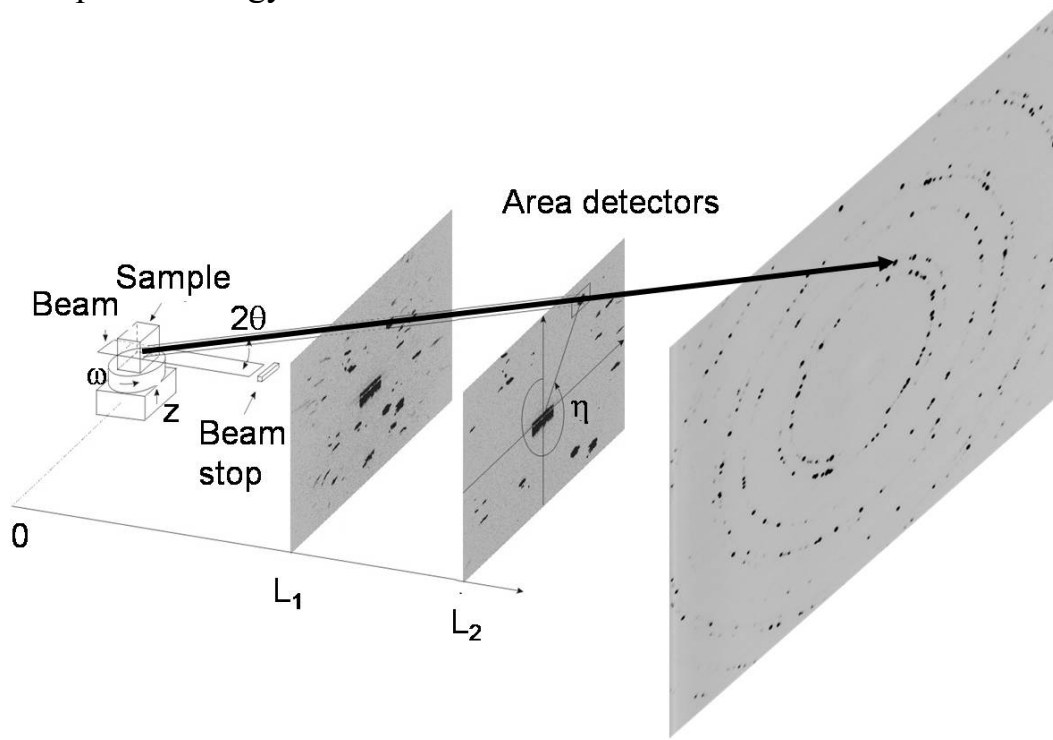


**Figure 1**

Sketch of the 3DXRD principle for the case of the incoming monochromatic beam illuminating one layer in the sample. Two types of detectors are used: high spatial resolution detectors close to the sample and low-resolution detectors far away from the sample. The Bragg angle  $2\theta$ , the rotation angle  $\omega$  and the azimuthal angle  $\eta$  are indicated for the diffracted beam arising from one grain of a coarse-grained specimen, and for a set-up with two high-resolution-detectors. The axes for the laboratory co-ordinate system are also shown.

The basic 3DXRD set-up – sketched in Fig 1 - is quite similar to conventional tomography settings at synchrotrons. A (nearly) parallel monochromatic X-ray beam impinges on the sample as a uniform field. The sample is mounted on a  $\omega$  rotation stage, where  $\omega$  is the rotation around an axis perpendicular to the incoming beam. As an option x-, y-, and z-translations may be added as well as additional rotations.

Any part of the illuminated structure, which fulfils the Bragg condition, will generate a diffracted beam. This beam is transmitted through the sample and probed by a 2D detector. To probe the complete structure, and not just the part that happens to fulfil the Bragg condition, the sample is rotated. Hence, exposures are made for equi-angular settings of  $\omega$  with a step of  $\Delta\omega$ . To provide a uniform sampling the sample is rotated by  $\Delta\omega$  during each exposure. Essential to 3DXRD is the idea to mimic a 3D detector by positioning several 2D detectors at different distances,  $L$ , to the centre-of-rotation and exposing these either simultaneously (many detectors are semi-transparent to hard X-rays) or subsequently.

Presently, two types of detectors are used: near-field detectors (fluorescence screens combined with magnifying optics and a CCD camera) with a spatial resolution of 3-10  $\mu\text{m}$  in close proximity to the sample and far-field detectors with a resolution of 100-200  $\mu\text{m}$ . Typical  $L$  values are 2-10 mm and 20-50 cm, respectively. The former provide information on position and orientation degrees of freedom, while the latter probes strain and orientation as we will see later. With the near-field detectors, images may be acquired at several – typically 2 or 3 – distances as illustrated in Fig 1. This enables ray-tracing of the diffracted beam, also known as *tracking*.

The incoming beam may illuminate the full sample or be focused in one direction to probe only a layer within the material (see Fig 1). In the following we shall refer to these as the 3D and 2D case, respectively. Notably, the 2D case is restricted to use at third generation synchrotron sources, while the 3D case also applies to second-generation sources and in favourable cases even to work with laboratory sources. In the 2D case, 3D information is generated simply by repeating data acquisition for a set of layers and stacking the resulting reconstructions. The data analysis for this case is presently more mature, but ultimately the 3D case promises a better time resolution.

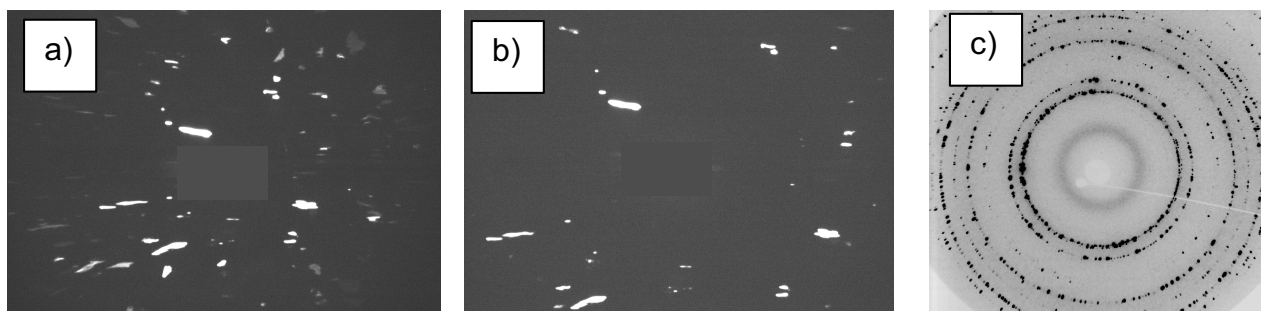


**Figure 2**

Typical 3DXRD data from a coarse-grained undeformed polycrystal. (a) and (b) are “near-field” exposures with high-spatial-resolution detectors (see Fig. 1) at distances of  $L = 4$  mm and  $L = 8$  mm, respectively. The background is shown as black. (c) is a corresponding “far-field” image made with the low-resolution detector at  $L = 400$  mm and with the background shown as grey.

An example of a set of exposures obtained in the 2D case is provided in Fig 2. Note that in the near-field images the spots are extended (comprising information on grain shape) and form no clear pattern on the detector as their position is determined by Bragg’s law as well as by the positions of the associated grains within the sample. In contrast, in the far-field image the spot sizes are instrumentally limited. The positions of grains within the sample now make a negligible contribution to the positions of the spots. Hence, the spots are positioned on a set of Debye-Scherrer rings, similar to the case of conventional powder diffraction.

A vital difference between the two types of detectors relates to data acquisition time: with the current technology the far-field detectors are much more efficient than the near-field ones, and hence provide a time resolution that is several orders of magnitude better. This makes it necessary to carefully consider the priority of time and space resolution in a 3DXRD experiment. In practice we may distinguish between four modes of operation, as sketched in Fig 3.

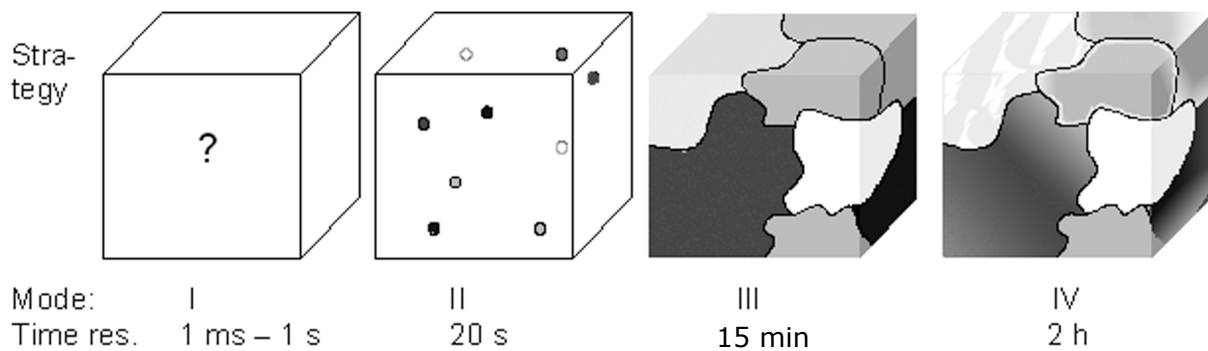


**Figure 3**

Sketch of four typical 3DXRD modes of operation. From right to left these are listed in direction of decreasing spatial information: (a) Mode IV: 3D orientation map of a deformed sample, (b) Mode III: 3D grain map for undeformed specimens, (c) Mode II: only center-of-mass position, volume, average orientation and average values of strain tensor elements for each grain, (d) Mode I: not all grains within the illuminated volume are probed. Furthermore, the information about orientation and position of those probed is not complete. In all cases, orientations are represented by the grey scale. Typical data acquisition times for characterisation of 100 grains are indicated

Modes I and II aim at fast data acquisition with limited spatial information. In Mode II for each grain in the illuminated part of the specimen, one can determine its center-of-mass position, volume, average orientation and average strain tensor. Mode I is an option for very fast measurements, where only a subset of all grains is characterised and no spatial information is available. Also, the orientation and strain characterisation will not be complete. Experimentally the main difference between the modes I and II is the  $\omega$  range covered.

Mode III and IV aim at generation of complete 3D maps. In case of an undeformed material, the orientation is constant within each grain, and the aim is to provide a *grain map*. In case of a deformed material, the orientation varies locally. This makes it relevant to measure *orientation maps*, where each voxel in the sample is associated with its own orientation. In both cases, evidently a high-spatial-resolution detector is needed.

In many experiments combinations of these modes are relevant. As an example one may wish to start by mapping extended parts of a sample in order to identify sub-volumes of particular interest. Then one focuses on such parts and performs a fast center-of-mass study on these parts during *in situ* processing. This procedure is then complemented by mapping extended parts again after the processing is completed. Also, center-of-mass type information from mode II is often needed to initialise reconstruction algorithms for grain and orientation mapping in mode III and IV, as explained in further detail below.

## 2. Indexing and characterization of average properties of each grain (modes I and II)

### Polycrystal indexing (mode II)

A very important simplification arises in the case where the diffraction pattern is composed of a set of (primarily) non-overlapping diffraction spots. Three examples of such data-sets are shown in Fig.

2. In this case, the diffraction spots can be sorted with respect to element of origin, say the grain, by means of a polycrystalline indexing scheme [6]. Based on this a comprehensive structural analysis of the average properties of each grain is readily available [7].

The starting point for such schemes is to apply image analysis routines which identify the spots and determine their center-of-mass positions in  $(y_{\text{det}}, z_{\text{det}}, \omega)$ -space, where  $y_{\text{det}}$  and  $z_{\text{det}}$  are the detector coordinates. Next, the direction of the corresponding diffracted X-rays are determined. In case of near-field data – that is the tracking set-up illustrated in Fig 1 – ray tracing may be used. Having identified a set of spots at different detector-to-sample distances which belong to the same reflection, the best fit to a straight line through the center-of-masses of these spots is determined. In case of far-field data one may simply assume that all grains are positioned at the center-of-rotation and for any spot draw the line from its center on the detector to the rotation axis. In both cases, once the direction of the ray is known, the corresponding scattering vector is readily determined.

The sorting/indexing can be based on three principles:

- *Orientation.* For each scattering vector, we can determine a line in 3D orientation space: the projection line. By definition the orientation of the associated grain is on this line. Furthermore, the projection lines for all the scattering vectors belonging to a given grain will intersect in one point. Hence, determining orientations becomes a question of finding intersections. This is an exercise in discrete tomography. Combinatorial methods (where one tests whether a set of spots forms a pattern consistent with the crystallographic symmetry) may be used, but only when the number of grains is small. Instead, the intersections can be found by scanning orientation space and for each orientation comparing a simulated diffraction pattern with the one observed experimentally [6].
- *Grain volume.* The integrated intensity of any diffraction spot is proportional to the volume of the associated grain. Having normalised intensities appropriately, as discussed in [1,8], all diffraction spots associated with a given grain should exhibit integrated intensities corresponding to the same volume within experimental noise.
- *Position.* In case of the use of ray tracing, the diffraction spots can be sorted according to position as well. To do so, the fitted X-ray line is extrapolated to the sample. In this way, in the 2D case, the  $(x,y)$  center-of-mass of the associated illuminated grain section is determined. In the 3D case, the sorting criterion is that the extrapolated lines all intersect in one point, namely the  $(x,y,z)$  center-of-mass of the associated grain.

The first polycrystal indexing program was GRAINDEX [6], which assumed a single-phase sample with a known crystallographic space group. This program has been replaced by Grainspotter, a part of the FABLE package [44]. In Grainspotter sorting is mainly based on orientations, but positions are taken into account. At the time of writing, Grainspotter is being generalised to unknown space groups and to multi-phase analysis. An alternative indexing program, based primarily on position information and relying on the use of Friedel pairs is described by Ludwig et al. [48].

Based on the output of the polycrystalline indexing program, a comprehensive characterisation of each grain immediately follows. If only the far-field detector is used the grain volume, average orientation and the average values of the components of the elastic strain tensor [10,49] can be determined. The time resolution is often  $\sim 1$  minute, limited by the read-out time of the detector. The accuracy is of order  $0.05^\circ$  for orientations and  $\Delta\varepsilon/\varepsilon \approx 10^{-4}$  for strain. Furthermore, it is possible to perform a full crystallographic analysis of each grain, e.g. a structural refinement [9,11].

In a variant of mode II also the centre-of-mass position of each grain is determined. At the expense of time resolution, this can be done by tracking using a high-spatial-resolution detector as outlined above. To determine positions with high accuracy, a non-linear least square fit to the CMS positions of the spots on the detector is performed. The accuracy is currently  $\sim 2 \mu\text{m}$ . Alternatively, for large grains with a size comparable to the resolution of a far-field detector, the same type of fit can also be applied to spot positions on such a detector. This alternative allows faster data acquisition than tracking but the resulting center-of-mass positions of the grains are less accurate (currently  $\sim 10 \mu\text{m}$ ).

Notably, the combined knowledge of the centre-of-mass position and volume of the grains can be used for a primitive tessellation, of sufficient quality to identify which grains are neighbours.

A large number of problems within polycrystal and powder research can be tailored to apply to mode II analysis. The main limitation is the probability of spot overlap on the detector. The probability is determined by the number of grains, the texture (the probability of grains exhibiting similar orientations), and the orientation spread of each grain. Simulations show that for samples with a weak texture and grains with a near-perfect lattice – that is with an orientation spread of order  $0.1^\circ$  or less - several thousand grains can be indexed simultaneously [9]. On the other hand, plastic deformation introduces orientation spread within the grains, which in practice prohibits indexing of embedded grains in materials that are deformed to more than 20%.

An example of data from a recent data set is shown in Fig 4.

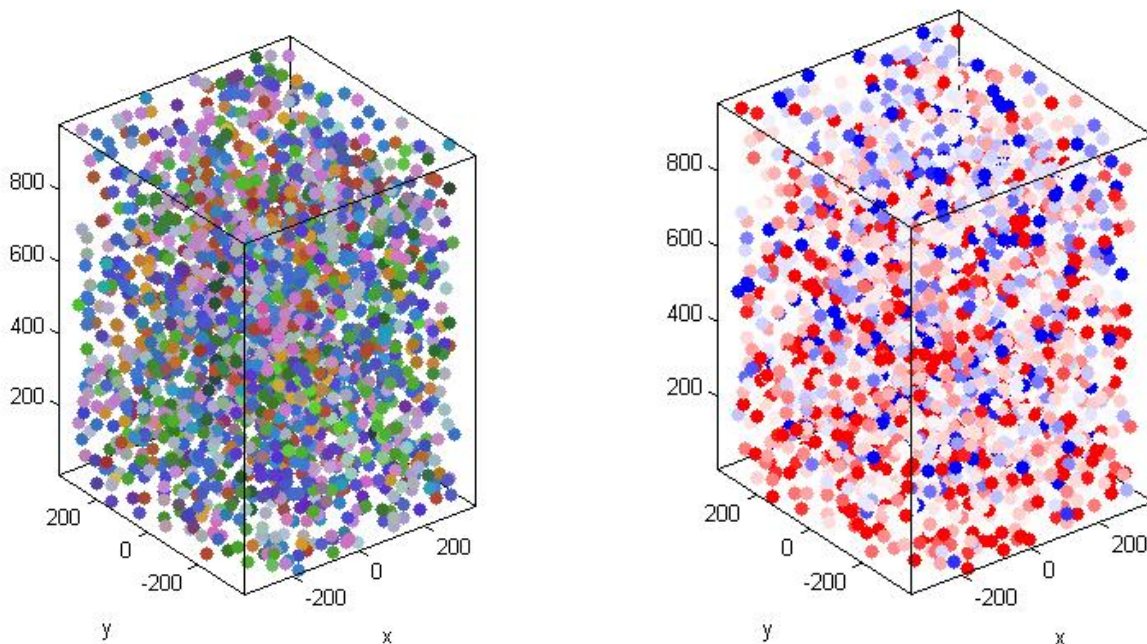


**Figure 4**

Maps of 2041 grains within a square steel sample with side length of  $700 \mu\text{m}$ . The illuminated height is 1 mm. Left: the colour code represents orientations of the grains. Right: the colour code represents axial strain values, blue symbolising compression and red tension. Courtesy of Oddershede.

### A statistical description of dynamics (mode I)

For very fast data acquisitions mode I is relevant. In this case, one simply repeats acquisitions with the far-field detector, oscillating around a given  $\omega$  setting. Assuming grains do not rotate, one can then monitor the change in volume of the grains giving rise to diffraction spots at this  $\omega$  setting. Several hundreds so-called *growth curves* can be obtained simultaneously in this way [12]. (To ensure that the integrated intensities monitored are truly proportional to corresponding grain volumes it is required at to validate the spots at regular intervals, e.g. by comparing intensities obtained at a nominal setting of beam size and rotation range,  $\Delta\omega$ , and a larger test setting of beam size and  $\Delta\omega$ . For more information on deriving growth curves see [8,12]). Notably one only probes a fraction of all the grains in the illuminated volume in this way, so the analysis is statistical in nature. Another limitation is that only components of the orientation and strain tensor are measured.

### Application I: Nucleation and growth studies

Traditionally, nucleation and growth phenomena have been analyzed using ensemble average properties, such as the volume fraction of transformed material. However, the predictive power of average properties is limited by the neglect of heterogeneities. For example, nucleation may take place preferentially at specific sites, and the growth rate of nuclei may depend strongly on orientation, size, stoichiometry, or relationships with neighbouring volumes. 3DXRD is an ideal tool to study the effect of heterogeneities, and as such it has been used for a series of studies related to recrystallization [8,12], solidification [13], and phase transformations in steel, ceramics and ferro-electrics. In all cases it was demonstrated that the ensemble average “Avrami-type” models are at best gross simplifications.

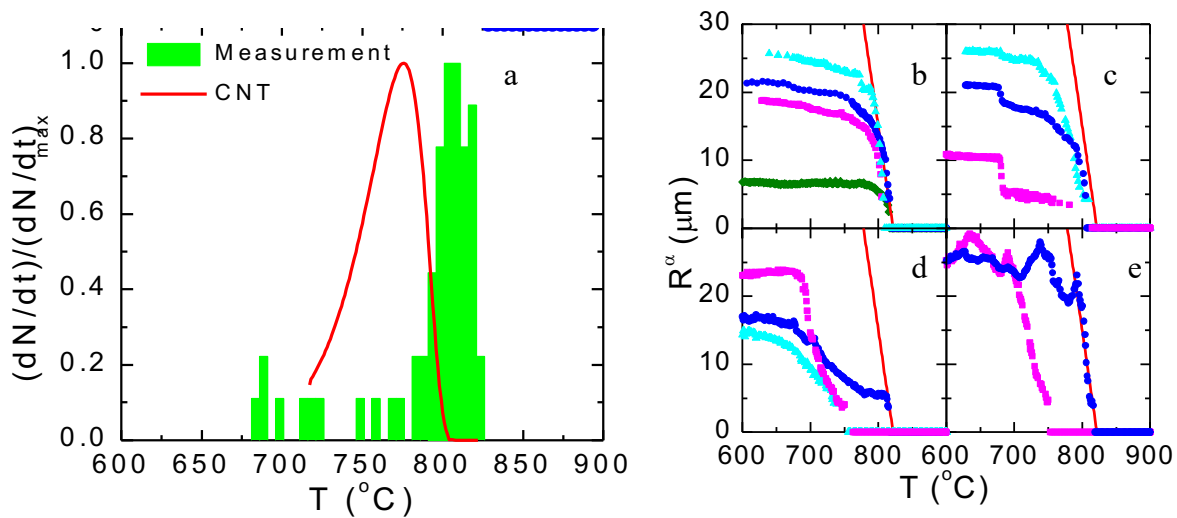


**Figure 5**

(a) Nucleation of ferrite grains during cooling of a carbon steel. The normalised observed nucleation rate (bars) is compared to theoretical prediction (line) based on a classical model [15]. (b-e) Examples of growth curves for individual ferrite grains, each being represented by one of the curves: (b) comprises ferrite grains that started to grow according to Zener theory, (c) ferrite grains that continued to grow with the same crystallographic orientation during pearlite formation at  $\sim 685$  °C as part of a pearlite colony, (d) ferrite grains that exhibited retarded growth due to a soft impingement and (e) ferrite grains that exhibit complex growth, perhaps due to a combination of hard and soft impingement. The lines are predictions from the parabolic growth model by Zener. From [14].

As an example of a 3DXRD study in mode I Offerman *et al.* have studied the phase transformation from the high-temperature austenite to the medium-temperature ferrite phase in carbon steel *in situ*

[14]. The results shown in Fig 5 relate to a study where the steel was cooled at a constant rate from 900 °C to 600 °C over 1 hour. During this process nucleation and growth of ferrite grains was inferred from the appearance and evolution of ~60 distinct diffraction spots originating from the ferrite. By simply counting the number of new spots appearing in a given time interval the nucleation rate is determined as function of temperature – a parameter that cannot be determined with high fidelity in any other way. In Fig 5 a) the nucleation rate is compared to a prediction from a classical nucleation model based on two assumptions: that the driving force for nucleation – the decrease in Gibbs free energy – can be determined from thermodynamic reference data, and that the nucleus is shaped as a pillbox with coherent and semi-coherent interfaces [15]. From analysis of the data shown in the figure it is found that the predicted and measured activation energies differ by more than two orders of magnitude. Relevant revisions to the model are currently being discussed.

Shown in Fig 5 b)-e) are examples of resulting growth curves for the nuclei. It appears that the growth of some grains – those in b) – followed closely the predictions of Zener, while others displayed large discrepancies. The latter was explained by several effects including local enrichment in the carbon content of the austenite.

## Application II: Plastic deformation

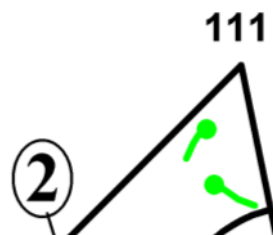


**Figure 6**

Rotation of the tensile axis of 95 grains within an Al specimen, as expressed in a stereographic triangle (a way of representing orientation space: grains near the corner marked “100” has the tensile axis close to the crystallographic (100) axis of the grain). The curves are the observed paths for the average orientation of each grain during tensile deformation from 0% to 6%. The final orientation is marked by a circle. The rotation behaviour is interpreted in terms of 4 regions marked by solid lines. From [18].

Polycrystal deformation is a topic of prime interest to both metallurgists and geoscientists. However, despite 70 years of effort, there is no consensus on how to approach the modelling. In particular, it is unclear to what extent deformation behaviour is determined by the initial grain orientation, the grain-grain interactions or by the emerging dislocation structures. 3DXRD provides *in situ* methods

for addressing these issues, for example through real-time observations of grain rotations in bulk materials during the deformation process [16,17]. As an example of 3DXRD work in mode II, Fig 6 provides a mapping of the rotation path of 95 grains in a 4-mm-thick polycrystalline Al sample strained in tension. These data provide a detailed combinatorial database for critical evaluation of models for polycrystalline deformation. In major parts of the orientation triangle, the paths exhibit a clear dependence on initial orientation. It is found that the grain responses do not match predictions from classical Taylor, Sachs or self-consistent models, but can be described by sub-dividing orientation space in four regions with distinctly different rotation behaviour [18].

### **Application III: Studies of sub-grains and nano-crystalline materials**

Notably, 3DXRD studies are also relevant for crystalline structures with a grain size smaller than the spatial resolution. Evidently, in such cases the generation of a grain map is not possible. However, by focusing the beam to say  $3 \times 3 \mu\text{m}^2$ , diffraction spots from individual grains as small as 30 nm can be detected. By tracing the integrated intensities and positions of such spots as function of time, one can infer changes in the volume, orientation and strain of the grains of origin.

The main limitation for such studies is spot overlap. To overcome this problem two approaches have been pursued. The first approach is based on reducing the number of illuminated grains by investigating foils [19]. Provided the foil thickness is at least 10 times the grain size, for many annealing processes the grains at the centre of the foil may be considered bulk grains. This methodology has been applied to a series of mode I and II coarsening studies of sub-grains in aluminium deformed to both medium and very high strains.

The second approach is to increase the angular resolution of the instrument by 2 orders of magnitude - to  $0.004^\circ$  in  $\eta$  and  $\omega$  and  $0.0005^\circ$  in  $2\theta$ . Implemented at sector 1-ID at APS, this improvement is achieved at the expense of flux by use of a six-bounce monochromator and a detector positioned at a distance of 4 m from the sample [20]. This set-up is designed specifically for studies of dislocation patterning. When deforming metals, typically the dislocations assemble into walls separating nearly perfect dislocation-free crystals – the subgrains – with dimensions of 100 nm to 2  $\mu\text{m}$ . With the set-up at APS individual spots from millions of illuminated subgrains in a 300  $\mu\text{m}$  thick Cu sample can be resolved. Full 3D reciprocal space maps are gathered continuously while deforming the specimen. Uniquely, from their time-dependence fundamental questions can be addressed in a direct way, such as “How and when do the dislocation structures form?” and “How do the structures subdivide as function of increasing strain?” In the case of tensile deformation of Cu, it is found that the dislocation structures form just after the plastic on-set and that the structures display intermittent dynamics – a surprising fact not predicted by theory [20].

### **3. Mapping of grains within undeformed specimens (mode III)**

Mapping grains in undeformed specimens can naturally be divided into two parts: identification of the number of grains and their orientations, and determination of the spatial position of grain boundaries, i.e. their morphologies. Provided spot overlap is not too severe an indexing program like Grainspotter can handle the first part.

Mapping is conceptually different for the 2D and 3D case. In the *3D case*, the intensity acquired in a given pixel on the detector is a line-integral: a sum of contributions from positions forming a line in the grain. Hence, mathematically speaking the problem is analogue to a range of well-known inverse problems, e.g. in classical tomography. Applying reconstruction principles to solve such problems is clearly relevant.

In the *2D case* with ideal optics and an ideal detector, any diffraction spot will be a projection of the boundary of the associated illuminated grain section. The projection implies that the contour of the grain boundary is demagnified in the direction along the beam by a factor of  $\sin(2\theta)\cos(\eta)$ . Hence, in principle the shape of any grain can be retrieved by back-projecting the periphery of one selected diffraction spot and correcting for the demagnification [7]. Unfortunately, the algorithm is associated with a spatial resolution along the direction of the incident beam which is one order of magnitude worse than in the transverse direction.

This problem can be overcome once more by applying a reconstruction approach. Hence, during the last years a number of reconstruction approaches have been suggested [21-26]. It is found that the task of performing such reconstructions is inherently different from absorption contrast tomography, as the number of projections in the latter case can be determined at will by adjusting the angular step. By contrast, in 3DXRD, the number and directions of projections giving rise to non-zero intensities are given by the crystallography. In practice only 5-20 projections may be of sufficient quality.

Below we list three 2D approaches, all of which have been implemented in code optimised for data processing speed (corresponding work on algorithms for the 3D case is currently undergoing (*e.g.* [22])):

- *Forward projection* In their most basic implementation forward projection programs simply scan over the grid of pixels in the sample and for each pixel orientation space is scanned to test which orientations match the diffraction patterns. Cross-talk between pixels in the layer is neglected. Hence, one can only infer the set of *possible* orientations. However in practice, the constraint that all pixels belonging to a given grain must have the same orientation often implies that there is one and only one (possible) orientation for each pixel. If that is not the case – *e.g.* in cases with substantial spot overlap – the ambiguous result may be used as input for inverse methods presented below. Two forward projections programs have been developed by R.M. Suter and co-workers [23] and S. Schmidt [24], respectively. The latter program is called GRAINSWEEPER. In this the search for possible orientations is performed by a discrete tomographic approach. This algorithm has been applied to a number of real data sets, see *e.g.* Fig 8 below.
- *Reconstruction based on ART.* An algebraic reconstruction method, ART, is presented in detail in [21]. It assumes that the orientations and approximate centre-of-mass positions of all grain sections are known *a priori*, *e.g.* determined by Grainspotter or GRAINSWEEPER. The method reconstructs the boundary of each grain separately, by solving a large set of linear equations iteratively. Once the solution has converged, the grain boundary can be defined by setting a threshold. A full grain map may be obtained by superposing the solutions – the boundaries – of the individual grains. However, such a map will not be space filling as boundaries from neighboring grains may overlap or leave “voids” in the map. To avoid this, one may choose for each pixel the grain where the reconstruction exhibited the largest density. First *experimental data* for 2D-ART were presented in [21].
- *Monte Carlo based reconstruction.* Stochastic approaches are attractive as they easily enable genuine simultaneous reconstructions of all grains rather than grain-by-grain reconstruction as 2D-ART above. On the other hand, speed of convergence is an issue. In the work by Alpers *et*

*al.* [25] and Rodek *et al.* [26] the Monte Carlo process is started by means of seeds: the center-of-mass position and orientation of each grain as determined by e.g. Grainspotter. Simulations have demonstrated superior properties of a Monte Carlo based approach, see [25], but at the time of writing the MC algorithms still have to be applied to real data.

The main limitation for grain mapping by 3DXRD is the instrumental point-spread-function of the near-field detector. The hard x-ray detectors used so far has lead to a spatial resolution of  $\sim 5 \mu\text{m}$ .

### Application I: Recrystallization

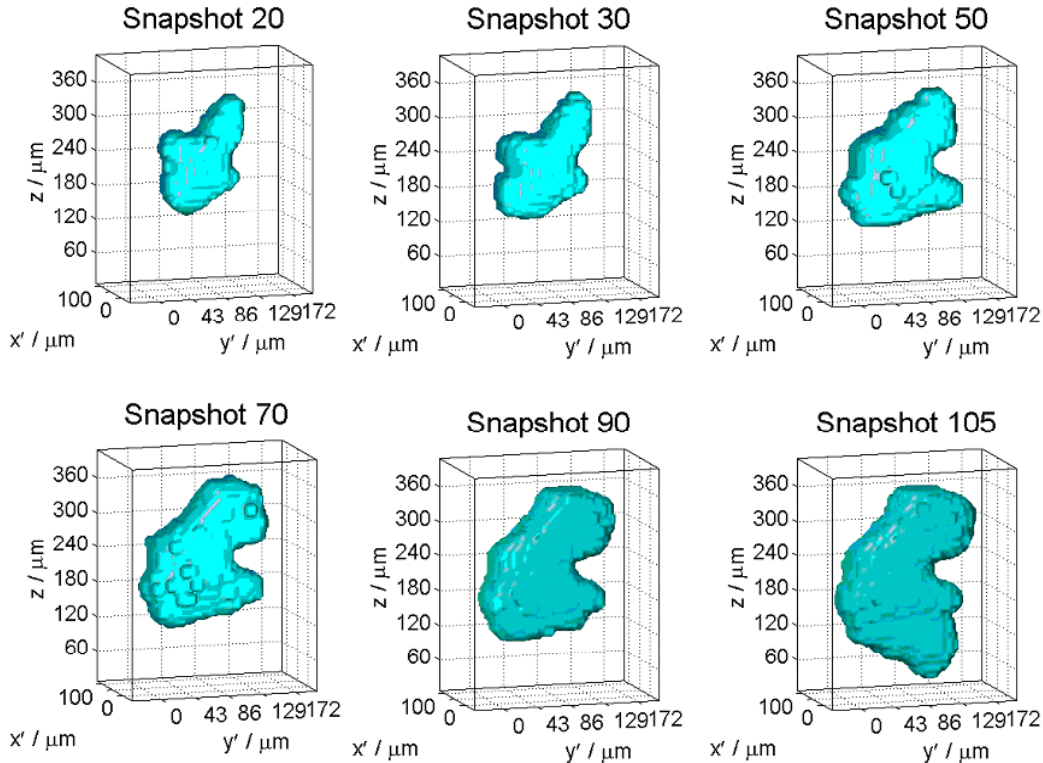


**Figure 7**

Storyboard visualising the growth of one emerging nucleus in an Al single crystal deformed by 42% as function of annealing. Selected snapshots are shown. From [27].

The first 3D movies of grain coarsening related to recrystallization [27], as it here – at least in the initial stage of the process – is relevant to visualise the growth of a single grain (nucleus). More specifically, nucleation in an aluminium single crystal deformed to 42% was stimulated by hardness indents. The crystal was subject to annealing for 30 hours at temperatures between 270 °C and 310 °C while being characterised *in situ*. The mapping comprised 50 z-layers with a spacing of 6  $\mu\text{m}$ . One emerging nucleus was identified at an early stage of the growth. Exposures were made around the  $\omega$  setting of a specific reflection belonging to this grain. The nucleus was mapped continuously with a time resolution of at most 10 minutes. Snapshots of the resulting 3D movie are shown in Fig 7. The data quality is sufficiently high so that two general features of growth are revealed:

1. Growth is very heterogeneous, so the shape is at times remarkably irregular.
2. Growth does not occur smoothly with time, but is often jerky.

These unique observations were explained by the heterogeneous nature of the deformed microstructure.

### Application II: Grain growth

Recently, Schmidt and co-workers performed the first grain growth study, where the evolution of the morphology of several hundred grains was monitored simultaneously [45]. A cylindrical Aluminium sample with a diameter of 700  $\mu\text{m}$  was mapped layer by layer within a total height of 350  $\mu\text{m}$  and with a resolution of  $\sim 10 \mu\text{m}$ . The sample was annealed in an external furnace. The grain volumes were reconstructed using the GRAINSWEEPER algorithm. In total, 5 annealing steps were made at annealing temperatures between 400  $^{\circ}\text{C}$  and 450  $^{\circ}\text{C}$ . Initially, 483 grains were present, while only 27 grains remained after the final annealing step. Examples of results are shown in Fig 8.

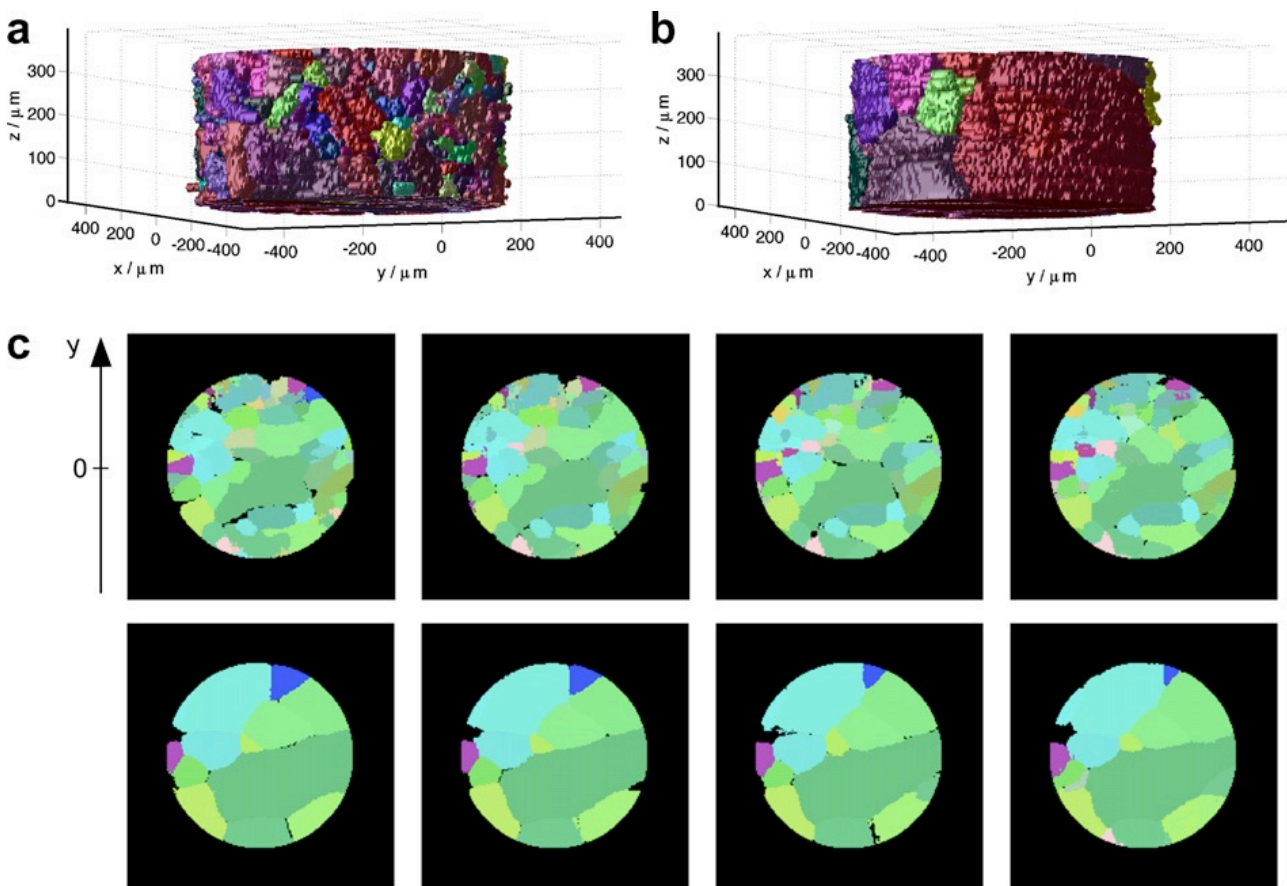


**Figure 8**

(a) The 3-D grain map resulting from the first annealing. (b) The same volume after the final annealing. (c) The four layers in the middle of the volume after the first annealing (top row) and the final annealing (bottom row). The interlayer spacing is 10  $\mu\text{m}$ . Colours symbolize crystallographic orientation. Black denotes vacancies, internal vacancies being an artefact of the program. The pixel size in the maps is 5  $\mu\text{m}$  x 5  $\mu\text{m}$ . From [45].

#### 4. Mapping of orientations within deformed specimens (mode IV)

For deformed specimens it is relevant to generate orientation maps, where each voxel in the specimen is associated with its own orientation, see Fig 3. In 2D such maps may be familiar as they are equivalent to the ones routinely generated by Electron BackScatter Diffraction (EBSD).

Establishing reconstruction algorithms for mode IV is considerably more challenging than mode III, the reason being that the configuration space is much larger for the deformed case than for the undeformed. Fortunately, the micro-structure exhibits additional properties, which may be exploited in the reconstruction. This is true in particular for *moderately deformed* specimens: that is specimens where the degree of deformation applied is sufficiently low that it still is possible to distinguish the boundaries of the (distorted) grains, although perhaps with some ambiguity. In particular, grains – whether distorted or not – exhibit the following properties

- (a) They are discrete, simply-connected 3D space filling objects
- (b) Their boundaries are smooth.
- (c) Their morphologies are not random.

It follows from this list that tools from the new discipline of discrete tomography [28] should be well suited for the reconstruction of grain maps.

##### Discrete tomography algorithm for moderately deformed specimens

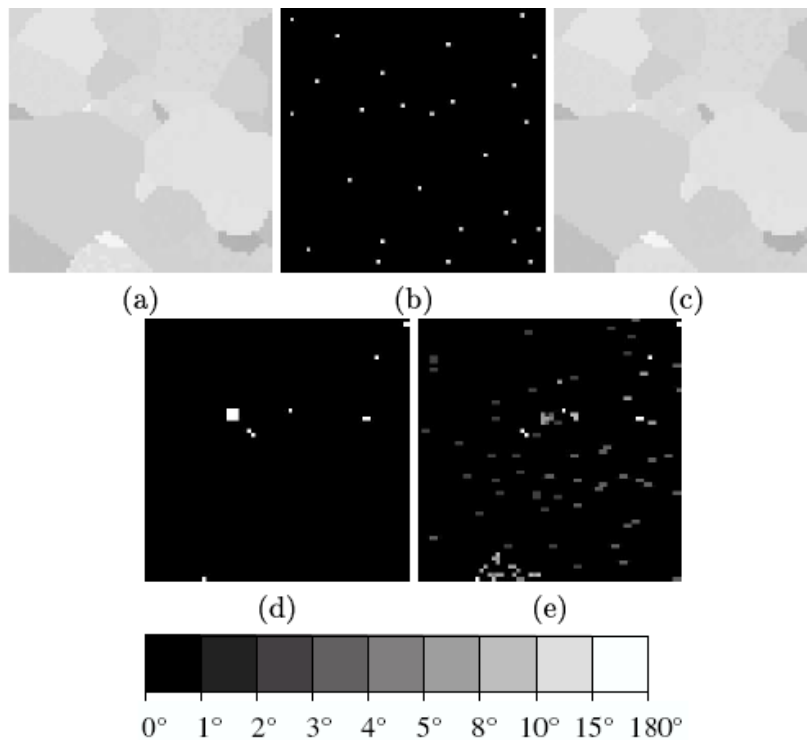


**Figure 9**

Reconstruction of a test case representing a deformed microstructure. (a): Reference orientation map, (b): seeds, (c): reconstructed orientation map. (d): Difference of the reference and the reconstructed grain maps. Black pixels denote identical grain labels, white pixels represent mismatching ones. (e): Difference of the reference and the reconstructed orientation maps. The brightness of the pixels is determined by the mis-orientation of corresponding orientation pairs, as shown in the grey scale key at the bottom of the figure. From [26].

Recently Rodek *et al.* presented an algorithm for moderately deformed specimens [26]. This is a Monte Carlo based approach where the discrete nature of the microstructure is used specifically. The routine assumes that prior information – arising *e.g.* from GRAINSWEEPER – makes it possible to identify the number of grains, and for each determine an approximate average orientation and one pixel in the layer which belongs to this grain. These points act as seeds for the algorithm.

In Ref [26] this approach is tested on a set of 64x64 pixel phantoms representing microstructures typical of various degrees of deformation. The results are encouraging. As an example in Fig 9 the reconstruction of a microstructure with 22 grains and with an internal orientation spread within grains of up to 22°. (In this reproduction of the maps (a) and (c) it is difficult to see the orientation gradient within the grains.) At low noise levels, the reconstructions based on comparison with the experimental data only were nearly perfect. At the time of writing analysis on real data is pending.

## 5. Diffraction Contrast Tomography (DCT)

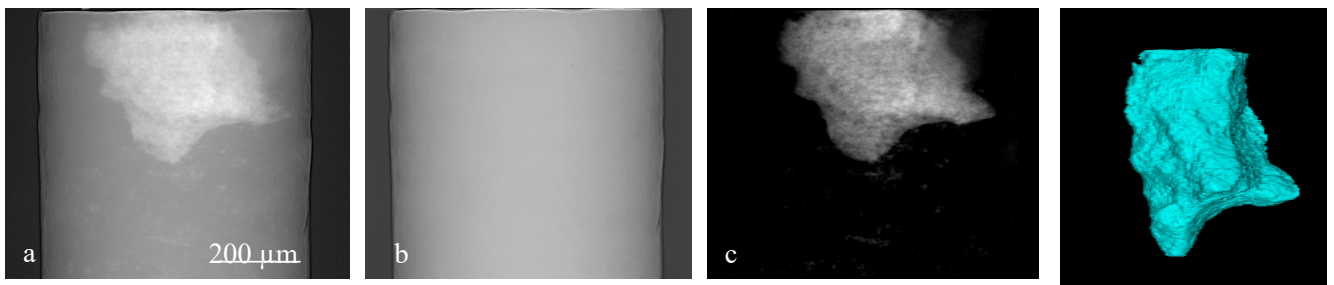


**Figure 10**

Diffraction contrast tomography: a) experimental projection with one grain fulfilling the Bragg condition, b) calculated absorption background, c) extracted grain projection, in all cases with brightness in image proportional to attenuation. d) reconstruction of 3D grain shape by means of algebraic reconstruction techniques. Courtesy of Ludwig.

DCT is an alternative approach for mapping grains in the sense of mode III above, developed by Ludwig and co-workers [46,47]. The principle is illustrated in Fig 10: assume a grain is in the Bragg-condition. Then there will be two contributions to attenuation of the direct beam: the absorption in the sample and the missing intensity due to diffraction. The latter additional contrast is clearly visible if the grains are near-perfect (mosaic spread well below 1 degree). Performing first a conventional reconstruction, a density map of the sample is obtained. Based on this one can simulate what the absorption data should look like for a non-crystalline sample. Subtracting the actual images from the simulated ones, one may sort the residual “grain contrast” images, based on a combination of real space (grain shape and position) and orientation space scanning procedures that compare simulated and measured angles. Having indexed a grain in this way, the 3D shape can be reconstructed based on the 3D-ART approach.

DCT and 3DXRD may be seen as the equivalent of “bright-field” and “dark-field” imaging in TEM. DCT has the advantage that a traditional tomography set-up can be used, and that the spatial resolution tends to be better (due to the detectors available). DCT has the drawback that the number of projections required needs to be much higher, of order of a few thousand images.

Combined dark-field and bright-field data sets have been acquired in several experiments at ID19 at ESRF. The results demonstrate that this combined method produce grain maps of superior resolution to those based on 3DXRD only. An example of results is shown in Fig 11. Here the spatial resolution was determined to be 2.5  $\mu\text{m}$ .

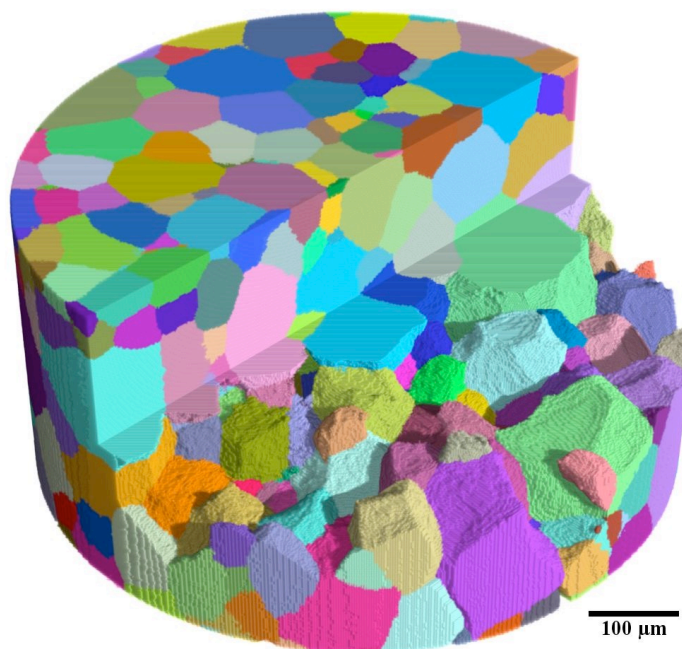


**Figure 11**

Grain map of  $\beta$ -Ti obtained by combined dark-field and bright-field reconstruction. To ease visualisation, the 3D map has been cut open. Colours represent orientations. Courtesy of Lauridsen.

Another variant of 3DXRD/DCT is *Topo-tomography*. This is a tomographic procedure, which allows reconstructing a single grain, using a set-up with additional tilt-stages [33]. For a selected grain, the scattering vector of a suited reflection is aligned parallel to the rotation axis of the tomographic setup. This particular setting assures that the diffraction condition is maintained while the sample is turned  $360^\circ$  around the rotation axis. Tomographic reconstruction can be performed from data acquired in direct and/or in diffracted beam by means of a standard (cone beam) filtered backprojection algorithm. In comparison to mode III reconstructions by 3DXRD above, the spatial resolution can be better. The disadvantage is the restriction to one grain only.

## 6. Combining 3DXRD, DCT and tomography

The 3DXRD set-up sketched in Fig 1 is very similar to the set-up typically used for parallel beam tomography. Furthermore it appears that the specifications of the two methods in terms of space and time resolution are not that different. Hence, it is relevant to attempt probing the same specimen with both techniques either simultaneously or consecutively. This combination is most interesting as diffraction and tomography utilise different contrast mechanisms. While 3DXRD is sensitive to variations in phase, orientation and elastic strain of crystalline materials, tomography is sensitive to density variations, independent of whether the material is crystalline or not.

The possible applications of combined 3DXRD, DCT and absorption/phase-contrast tomography data sets are numerous:

- The basic 3DXRD algorithms developed so-far all apply to mono-phase materials only. A combined data set enables the methodology to be extended to multi-phase materials, by first segmenting the volume to be reconstructed based on density and then applying the 3DXRD method to one phase at the time.
- On the macroscopic scale, the possibility of combining tomography and strain scanning has been realised by a number of authors [30,31]. On the mesoscale, the combination of tomography and 3DXRD is equally appealing. In particular, for fatigue and damage control studies one may investigate the interaction between propagating voids or cracks, the associated elastic strain fields and the grain or dislocation structures in the material.
- Recently a method has been demonstrated for characterisation of 3D plastic strain fields using X-ray tomography and embedded marker particles [32]. Strains in the range of 1% upwards can be mapped with a spatial resolution of  $\sim 20 \mu\text{m}$  within mm sized specimens. Combining plastic strain mapping with grain mapping by 3DXRD is a very powerful tool for studies of polycrystal deformation.

As an example of the comprehensive kind of mapping made possible by a combined study, in Fig 12 we show results from the work on stress corrosion cracking by King et al. [48]. Here, initially a grain map was made by DCT. Then crack propagation was observed *in situ* using tomography. By correlating position of the crack surface and the speed of the crack front with the grain morphologies and grain orientations new insight on the process was obtained.

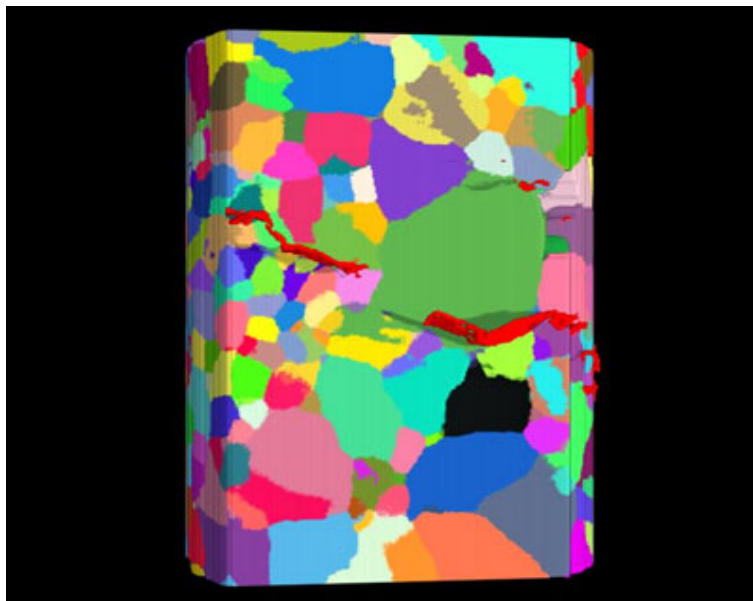


**Figure 12**

Combined DCT and tomography work on stress corrosion cracking. Rendering of the grain map (randomly coloured) and crack (red). The crack can be seen to propagate along the grain boundaries. The illuminated part of the cylindrical sample – with a diameter of  $400 \mu\text{m}$  – comprised some 360 grains. From [48].

## 7. 3DXRD microscopes and software

Currently there are four dedicated 3DXRD microscopes either in operation or in planning. These are all installed at 3<sup>rd</sup> generation synchrotrons sources and operate in the energy range 30-100 keV. The first was built at the Materials Science beamline ID11 at the ESRF in 2000, and has recently been upgraded [34]. At sector 1 at the APS [35] a similar instrument is installed; this beamline also offers the option for high angular resolution 3DXRD [20]. At the time of writing, a 3DXRD microscope – the GrainMapper – is becoming operational at the high energy materials science (HEMS) beamline at PETRA-III in Hamburg. Finally, Spring-8 in Japan has plans for such an instrument.

The majority of the existing 3DXRD related software has been developed within the framework of an EU program known as TotalCryst. The resulting open source software – the package known as FABLE - can be downloaded from the web [44].

### References

1. H. F. Poulsen. Three-Dimensional X-Ray Diffraction Microscopy. (Springer, Berlin, 2004)
2. B.C. Larson, W. Yang, G.E. Ice, J.D. Budai, and T.Z. Tischler (2002). *Nature* **415**, 887-890.
3. H.J. Bunge, L. Weislak, H. Klein, U. Garbe, and J.R. Schneider (2003). *J. Appl. Cryst.* **36**, 1240-1255
4. T. Wroblewski, O. Clauss, H.-A. Crostack, A. Ertel, F. Fandrich, Ch. Genzel, K. Hradil, W. Ternes, and E. Woldt (1999). *Nucl. Instr. Meth. A* **428**, 570-582.
5. MRS Bulletin, April 2004 issue.
6. E.M. Lauridsen, S. Schmidt, R.M. Suter, and H.F. Poulsen (2001). *J. Appl. Cryst.* **34**, 744-750.
7. H.F. Poulsen, S.F. Nielsen, E.M. Lauridsen, S. Schmidt, R.M. Suter, U. Lienert, L. Margulies, T. Lorentzen and D. Juul Jensen (2001). *J. Appl. Cryst.* **34**, 751-756.
8. E.M. Lauridsen, D. Juul Jensen, H. F. Poulsen, and U. Lienert (2000). *Scripta Mat.* **43**, 561-566.
9. S. Schmidt, H.F. Poulsen and G.B.M. Vaughan (2003). *J. Appl. Cryst.* **36**, 326-332.
10. R.V. Martins, L. Margulies, S. Schmidt, H.F. Poulsen, T. Leffers (2004). *Mater. Sci. Eng. A* **387-389C**, 84-88.
11. G.B.M. Vaughan, S. Schmidt, and H.F. Poulsen (2004), *Z. Kristall.* **219**, 813.
12. E.M. Lauridsen, H.F. Poulsen, S.F. Nielsen and D. Juul Jensen (2003). *Acta Mat.* **51**, 4423-4435.
13. N. Iqbal, N.H. van Dijk, S.E. Offerman, M.P. Moret, L. Katgerman, and G.J. Kearley (2005), *Acta Mater.* **53**, 2875-2880.
14. S.E. Offerman, N.H. van Dijk, J. Sietsma, S. Grigull, E.M. Lauridsen, L. Margulies, H.F. Poulsen, M.T. Rekveldt, and S. van der Zwaag (2002). *Science* **298**, 1003-1005.
15. W.F. Lange III, M. Enornoto, and H.I. Aaronson (1988). *Metall. Trans.* **19A**, 427-440.
16. L. Margulies, G. Winther, and H. F. Poulsen (2001). *Science* **291**, 2392-2394.
17. H.F. Poulsen, L. Margulies, S. Schmidt, and G. Winther (2003). *Acta Mat.* **51**, 3821-3830.
18. G. Winther, L. Margulies, S. Schmidt and H. F. Poulsen (2004). *Acta Mat.*, **52**, 2863.
19. C. Gundlach, W. Pantleon, E.M. Lauridsen, L. Margulies, R. Doherty, and H.F. Poulsen (2004), *Scr. Mater.* **50**, 477-481
20. B. Jakobsen, H.F. Poulsen, U. Lienert, J. Almer, S.D. Shastri, H.O. Sørensen, C. Gundlach, and W. Pantleon (2006). *Science*, **312**, 889-892.
21. H.F. Poulsen and X. Fu (2003). *J. Appl. Cryst.* **36**, 1062-1068.
22. T. Markussen, X. Fu, L. Margulies, E.M. Lauridsen, S.F. Nielsen, S. Schmidt, and H.F. Poulsen (2004). *J. Appl. Cryst.* **37**, 96-102.

23. R.M. Suter, D. Hennesy, C. Xiao, U. Lienert. *Rev. Sci. Instrumen.* **77**, 123905.
24. S. Schmidt, preprint.
25. A. Alpers, H.F. Poulsen, E. Knudsen, and G.T. Herman (2006). *J. Appl. Cryst.* **39**, 582-588
26. L. Rodek, H.F. Poulsen, E. Knudsen, G.T. Herman (2007). *J. Appl. Cryst.* **40**, 313-321.
27. S. Schmidt, S.F. Nielsen, C. Gundlach, L. Margulies, X. Huang, D. Juul Jensen (2004). *Science*, **305**, 229-232.
28. G.T. Herman, A. Kuba, eds. (1998): *Discrete Tomography* (Birkhäuser, Boston)
29. H.F. Poulsen (2003). *Phil. Mag.* **83**, 2761-2778.
30. M. Preuss, P.J. Withers, E. Maire, and J.Y. Buffiere (2002). *Acta Mater.* **50**, 3177-3192
31. A. Pyzalla, B. Camin, T. Buslaps, M. Di Michiel, H. Kaminski, A. Kottar, A. Pernack, W. Reimers (2005). *Science* **308**, 92-95.
32. S.F. Nielsen, H.F. Poulsen, F. Beckmann, C. Thorning, and J.A. Wert (2003). *Acta Mat.* **51**, 2407-2415.
33. W. Ludwig, P. Cloetens, J. Härtwig, J. Baruchel, B. Hamelin, P. Bastie (2001). *J. Appl. Cryst.* **34**, 602-607.
34. [www.esrf.fr](http://www.esrf.fr);
35. [beam.aps.anl.gov/pls/apsweb/beamline\\_display\\_pkg.display\\_beamline?p\\_beamline\\_num\\_c=30](http://beam.aps.anl.gov/pls/apsweb/beamline_display_pkg.display_beamline?p_beamline_num_c=30)
36. B.E. Warren (1990). *X-ray diffraction. Springer Tracts in Modern Physics* (Dover, New York).
37. J. Als-Nielsen and D. McMorow (1999). *Elements of X-ray Physics* (Wiley, New York).
38. C. Giacobozzo, H.L. Monaco, D. Viterbo, F. Scordari, G. Gilli, G. Zanotti, and M. Catti. *IUCr Texts on Crystallography 2: Fundamentals of Crystallography* (Oxford University Press, Oxford).
39. U.F. Kocks, C.N. Tome, and H.R. Wenk (1998). *Texture and Anisotropy* (Cambridge University Press, Cambridge).
40. A. Morawiec (2004). *Orientation and Rotations, Computations in crystallographic textures.* (Springer, Berlin).
41. H.J. Bunge (1969). *Matematische Methoden der Texturanalyse* (Akademie Verlag, Berlin).
42. F.C. Frank (1988) *Metall. Trans A.* **19**, 403.
43. A. Morawiec and D.P. Field (1996). *Philos. Mag.* **A73**, 1113-1130
44. <http://fable.wiki.sourceforge.net/>
45. S. Schmidt, U.L. Olsen, H.F. Poulsen, H.O. Sørensen, E.M. Lauridsen, L. Margulies, C. Maurice, D. Juul Jensen (2008). *Scripta Mater.* **59**, 491-494.
46. W. Ludwig, S. Schmidt, E.M. Lauridsen, H.F. Poulsen (2008). *J. Appl. Cryst.* **41**, 302-309.
47. W. Ludwig, P. Reischig, A. King, M. Herbig, E.M. Lauridsen, G. Johnson, T.J. Marrow, J.Y. Buffière (2009). *Rev. Sci. Instrum.* **80** 033905
48. A. King, G. Johnson, D. Engelberg, W. Ludwig, and J. Marrow, *Science* (2008) **321**, 382 – 385
49. J. Oddershede, S. Schmidt, H. F. Poulsen, H. O. Sørensen, J. Wright, and W. Reimers, *J. Appl. Cryst.* (2010) **43(3)**, 539-549.